

RESEARCH

Open Access



# Indacenodithienothiophene-based A-D-A-type phototheranostics for immuno-phototherapy

Yangtian Ye<sup>1</sup>, Shaojing Zhao<sup>2</sup>, E Pang<sup>2</sup>, Yuanyu Tang<sup>2</sup>, Pan Zhu<sup>2</sup>, Wenjie Gao<sup>3</sup>, Qingxu Diao<sup>4</sup>, Jie Yu<sup>4</sup>, Jie Zeng<sup>4\*</sup>, Minhuan Lan<sup>2\*</sup> and Jianing Yi<sup>4\*</sup>

## Abstract

The development of phototherapeutics with high photothermal conversion efficiency (PCE) and strong ability to generate reactive oxygen species under single near-infrared (NIR) laser irradiation for immuno-phototherapy applications remains a significant challenge. Herein, we optimally selected the molecule IT-4 F with an acceptor-donor-acceptor (A-D-A) structure to prepare water-dispersible nanoparticles (NPs) by assembly with DSPE-PEG-NH<sub>2</sub>. Such NPs have NIR absorption and fluorescence peaks at 728 and 817 nm, respectively. They can generate singlet oxygen (<sup>1</sup>O<sub>2</sub>) and superoxide anion (O<sub>2</sub><sup>-</sup>) under laser irradiation, with a <sup>1</sup>O<sub>2</sub> generation quantum yield of 31.5%. They can also effectively convert photon-energy into heat with a high PCE of 42.8%. The outstanding properties of IT-4 F NPs enable them to be used in NIR fluorescence imaging guided photothermal therapy (PTT), and photodynamic therapy (PDT). Moreover, PDT and PTT triggered immunogenic cell death and PANoptosis in tumor cells, which not only inhibited tumor growth and metastasis in mice model, but also induced a robust immune response, evidenced by increased infiltration of CD8<sup>+</sup> T cells, CD4<sup>+</sup> T cells, dendritic cells, and a decreased presence of immunosuppressive cells such as myeloid-derived suppressor cells and regulatory T cells. The efficacy of IT-4 F NPs in organoid of human breast cancer was also verified.

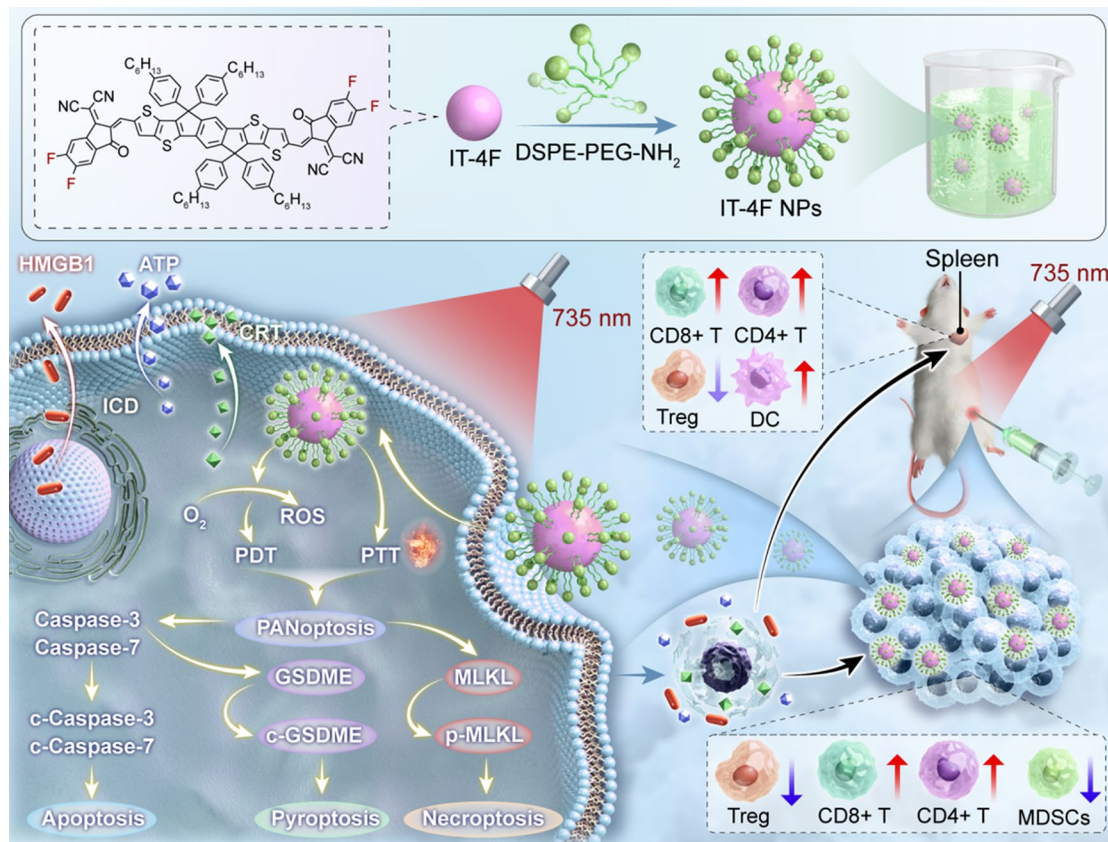
\*Correspondence:

Jie Zeng  
zengjie227@hunnu.edu.cn  
Minhuan Lan  
minhuanlan@csu.edu.cn  
Jianing Yi  
yijianing@hunnu.edu.cn

Full list of author information is available at the end of the article



© The Author(s) 2025. **Open Access** This article is licensed under a Creative Commons Attribution-NonCommercial-NoDerivatives 4.0 International License, which permits any non-commercial use, sharing, distribution and reproduction in any medium or format, as long as you give appropriate credit to the original author(s) and the source, provide a link to the Creative Commons licence, and indicate if you modified the licensed material. You do not have permission under this licence to share adapted material derived from this article or parts of it. The images or other third party material in this article are included in the article's Creative Commons licence, unless indicated otherwise in a credit line to the material. If material is not included in the article's Creative Commons licence and your intended use is not permitted by statutory regulation or exceeds the permitted use, you will need to obtain permission directly from the copyright holder. To view a copy of this licence, visit <http://creativecommons.org/licenses/by-nc-nd/4.0/>.

**Graphical abstract**

**Keywords** Photodynamic therapy, Photothermal therapy, Immunogenic cell death, PANoptosis, Human breast cancer

**Introduction**

Immunotherapy activated by photodynamic therapy (PDT), known as immuno-photodynamic therapy (IPDT), utilizes the high cytotoxic reactive oxygen species (ROS) generated by photosensitizers under laser irradiation to efficiently kill tumor cells in situ [1]. This process simultaneously releases tumor-associated antigens, thereby activating the immune system for effective treatment of distant and metastatic tumors. IPDT not only retains the advantages of PDT, such as high selectivity, no resistance, and minimal side effects, but also offers benefits such as reduced systemic toxicity, improvement of the tumor immunosuppressive microenvironment, and prevention of cancer recurrence through immune memory [2, 3]. Qu, et al. [4]. used PCPDTTBTT as the photosensitizer to design a novel light-responsive nano-platform that targets the pancreatic ductal adenocarcinoma (PDAC) tumor microenvironment (TME) using tumor-specific intermediate factor nanobodies (Nbs). Under laser irradiation, this platform generates ROS,

inducing tumor cell apoptosis and immunogenic cell death (ICD), ultimately preventing tumor progression and remodeling the immunosuppressive TME lymphocytes by increasing T cell infiltration. Similarly, Ren, et al. [5] designed a novel rhenium complex (Re-TTPY) capable of generating singlet oxygen ( $^1O_2$ ), superoxide anion ( $O_2^{\cdot-}$ ), and hydroxyl radical ( $\cdot OH$ ) under laser irradiation. This complex induces ferroptosis via PDT while triggering ICD and promoting the maturation of dendritic cells (DCs) and T cell infiltration. Overall, IPDT not only treats primary tumors but also promotes the infiltration of immune cells into tumors and enhances anti-tumor immune responses.

Photosensitizer plays a key role in the efficacy of IPDT. However, the generation of ROS in PDT is limited by the hypoxic nature of the TME [6, 7]. Hypoxia leads to metabolic reprogramming in tumor cells, impairing immune cell function and consequently affecting immune responses [8]. Additionally, immunosuppressive cells within the TME, such as M2 macrophages and regulatory

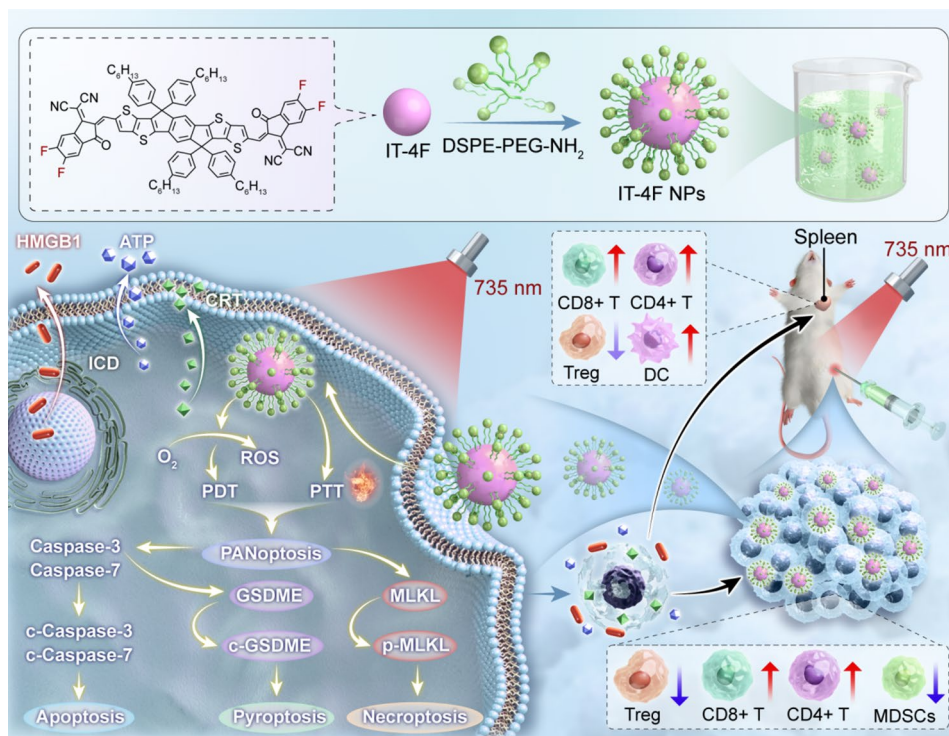
T cells (Tregs), can exacerbate this issue, suppressing anti-tumor immune responses [9, 10]. To overcome these challenges, various strategies have been proposed [11]. For example, to enhance oxygen supply to tumors and improve PDT efficacy, Li, et al. [12] developed an acidity-responsive biodegradable iridium-based (IPC) nanomedicine composed of iridium ions, chlorin e6 (Ce6), and polyvinylpyrrolidone. IPC accumulates at high levels in tumors, catalyzing excess hydrogen peroxide to produce oxygen while depleting intracellular glutathione in cancer cells. As a result, Ce6 is released, generating ROS more effectively upon laser irradiation. Moreover, IPC nanomedicines alleviate tumor hypoxia, amplifying PDT effects, inducing more ICD, and enhancing anti-tumor immunity by reversing the immunosuppressive TME. Similarly, Lan, et al. [13] developed a nanoscopic metal-organic framework, Fe-TBP, made of iron oxide clusters and porphyrin ligands. Fe-TBP can convert intracellular  $H_2O_2$  to  $O_2$  through the Fenton reaction, overcoming hypoxia, enabling PDT to generate  $^1O_2$  under both normoxic and hypoxic conditions. This leads to non-inflammatory tumor immunotherapy and significant infiltration of cytotoxic T cells. However, it is important to note that the single mode of cell death induced by PDT reduces tumor-specific antigens, limits the generation of in situ tumor vaccines, and reduces the diversity of regulatory immune cells, thus weakening the overall effect of IPT.

Recent studies reported that ROS generated during PDT can damage heat shock proteins, while the heat generated by photothermal therapy (PTT) can accelerate blood flow, thereby increasing oxygen concentration in the tumor region [14]. By combining PDT and PTT, it is possible to enhance the PDT treatment effect caused by oxygen, and leverage this synergy to promote ICD, further improving the efficacy of immune-phototherapy (IPT) for tumor treatment [15]. For example, Li, et al. [16] used PCPDTTBT as photosensitizer to integrate aggregation-induced emission luminogens (AIEgen) with Prussian blue (PB) nanocatalysts for powerful cancer immunotherapy. The dimethylamine-substituted AIEgen exhibited impressive near-infrared (NIR) laser-induced PDT capabilities and photothermal conversion. By incorporating AIEgen into porous PB NPs, followed by encapsulation in M1 macrophage membranes, a tumor-specific therapeutic and diagnostic nanomedicine was developed. This strategy effectively limits the molecular motion of AIEgen, thereby enhancing PDT efficiency and NIR fluorescence brightness. Additionally, PBNPs catalyze the generation of oxygen by decomposing the excess  $H_2O_2$  expressed in tumors, further enhancing PDT efficacy. The NIR absorption of PB also improves photoacoustic imaging and photothermal effects. Wu, et al. [17] designed a novel Ln@Fe nanoparticle composed of lanthanide-doped luminescent nanoparticles (LnNPs) conjugated

with Ce6 and  $Fe^{3+}$ -gallic acid (GA). GA mediates the reduction of  $Fe^{3+}$  to  $Fe^{2+}$ , which then participates in the Fenton reaction to generate  $\cdot OH$ . Laser excitation of Ce6 produces  $^1O_2$  for PDT. Furthermore, Fe-GA serves as a PTT agent, and the PTT process enhances ROS generation. Ln@Fe NPs not only improve the synergistic anti-tumor efficacy by promoting ROS generation, but also effectively inhibit tumor metastasis by activating robust anti-tumor immunity.

However, multifunctional therapeutic agents that combine photosensitizers and photothermal agents have drawbacks that make them unsuitable for practical applications. These include difficulties in controlling the ratio of active components, poor experimental reproducibility, and the need for multiple laser wavelengths for excitation [18]. Therefore, the design and synthesis of molecules that can simultaneously generate ROS and heat under excitation at a single NIR wavelength is of great significance for the development of IPT [19, 20].

Considering the strong NIR absorption capabilities of photovoltaic molecules [21], in this study, we assembled a molecule with an acceptor-donor-acceptor (A-D-A) structure, IT-4 F, and combined it with DSPE-PEG- $NH_2$  to prepare water-dispersible NPs for NIR fluorescence-guided IPT. As shown in Scheme 1, IT-4 F contains a large planar indacenodithienothiophene (IDTT) central unit acting as electron-donating fused-ring core, and a fluorinated 2-(3-oxo-2,3-dihydroinden-1-ylidene) malononitrile (INCN) as an electron-withdrawing unit. The A-D-A structure provides strong intramolecular charge transfer (ICT) and NIR absorption and fluorescence properties. Moreover, the alkyl chains effectively prevent  $\pi$ - $\pi$  stacking interactions between IT-4 F molecules. The assembly of the hydrophobic IT-4 F with the amphiphilic DSPE-PEG- $NH_2$  formed water-dispersible IT-4 F NPs which exhibited excellent photostability and biocompatibility, displaying intense NIR absorption and fluorescence with peaks at 728 nm and 817 nm, respectively. Moreover, the IT-4 F NPs effectively converted photon energy into heat with a photothermal conversion efficiency (PCE) of up to 42.8%, while generating  $^1O_2$  and  $O_2^{\cdot -}$  with a quantum yield for the generation of  $^1O_2$  of 31.5%, which is comparable with previous results as shown in Table S1. The study further validated the application of these NPs in PDT and PTT, leading to various forms of cell death, such as ICD and PANoptosis. PANoptosis refers to multiple cell death process that integrates pyroptosis, apoptosis, and necroptosis, collectively contributing to an inflammatory response that facilitates immune activation. This process promoted the generation of in situ tumor vaccines, and accelerated blood circulation, enabling the delivery of immune cells to peripheral immune organs, thus mobilizing and activating systemic immune cells. This in turn reshaped the TME and ultimately enhanced



**Scheme 1** Schematic representation showing the preparation and application of IT-4 F NPs

the capability of immuno-phototherapy to treat both primary and metastatic tumors. Lastly, the therapeutic efficacy of IT-4 F NPs was further assessed using organoids cultured from patient-derived tumor tissues. The IT-4 F NPs possess both PDT and PTT capabilities under a single near-infrared wavelength excitation, simplifying the treatment process compared to current nanomaterials that require multiple wavelength excitations. Moreover, IT-4 F NPs can trigger various forms of cell death, such as immunogenic cell death and PANoptosis. This work offers a novel approach to enhancing cancer treatment through the integration of photothermal and photodynamic effects, while also eliciting strong anti-tumor immunity, thus contributing significantly to the field of nanomedicine and cancer immunotherapy.

## Experimental section

### Materials

IT-4 F was purchased from Organtec Ltd. DSPE-PEG-NH<sub>2</sub>-2000 was purchased from ShangHai ToYongBio Tech. Inc. SOSG was purchased from Shanghai Maokang Biotechnology Co., Ltd. Dihydrorhodamine 123 (DHR 123), O22, and DHE probe were purchased from Beijing BioLab. Technology Co., Ltd. MTT was obtained from Sigma-Aldrich Trading. High mobility group protein B1 (HMGB1) and Calreticulin (CRT) antibody was purchased from ABclonal Biotechnology Co., Ltd. ATP Assay Kit was purchased from Beijing Beyotime

Biotechnology Co., Ltd. 4T1 cell line was purchased by Wuhan Servicebio Technology Co., Ltd. Anti-cleaved Caspase 3 antibody (CST), anti-cleaved GSDME antibody (CST), anti-cleaved Caspase 7 (CST), anti-pMLKL (S345) antibody (CST) were purchased by Cell Signaling Technology, Inc. Six-week-old female BALB/c mice were purchased by Hunan SJA Laboratory Animal CO.,LTD.

### Instruments

UV-vis spectra were obtained by a Shimadzu UV-2600 spectrophotometer. Fluorescence spectrum spectra were measured on an RF-6000 spectrophotometer. Scanning electron microscopy (SEM) images were captured from JSM-7610FPlus, JEOL Ltd. Particle size and zeta potential were obtained by a Malvern ZS particle size and zeta potential analyzer. Fluorescence cellular images were obtained under an inverted fluorescence microscope (Leica DMIL LED) and a CLSM (Leica SP8). MTT cell viability experiments were performed using an enzyme-labeled instrument (Varioskan LUX).

### Preparation of IT-4 F NPs

IT-4 F (3.0 mg) and DSPE-PEG-NH<sub>2</sub>-2000 (6.0 mg) were dissolved in 1.0 mL of tetrahydrofuran (THF). The mixture was slowly added to 20.0 mL of water while being ultrasonicated. Then, the solution was transferred to a dialysis bag (MWCO = 3500 DA) and dialyzed with magnetic stirring for 24 h, changing the water every 4 h to

remove excess DSPE-PEG-NH<sub>2</sub> and THF. An aqueous solution of IT-4 F NPs was obtained and stored in the dark at 4 °C.

#### Determination of singlet oxygen in IT-4 F NPs solution

1 μL of the SOSG were added to 2.0 mL of IT-4 F NPs solution (3.6 μM). The solution was irradiated with a 735 nm laser (1 W/cm<sup>2</sup>). The fluorescence spectra of SOSG were measured every 10 s. The fluorescence spectrum of SOSG in pure water was also measured under the same conditions.

#### Determination of superoxide anion in IT-4 F NPs solution

DHR 123 was used as superoxide anion detection reagent. 1 μL of DHR 123 was added to 2.0 mL of IT-4 F NPs solution (5 μM). The solution was irradiated with 735 nm laser (0.5 W/cm<sup>2</sup>). The fluorescence spectra of DHR 123 were measured every 10 s. The fluorescence spectrum of DHR 123 in pure water was also measured under the same conditions.

#### Determination of photostability of IT-4 F NPs solution

IT-4 F NPs solution (3.6 μM) was exposed to 735 nm laser (1 W/cm<sup>2</sup>) for 10 min. The absorption spectra of IT-4 F NPs solution were measured every minute. The absorption spectra of Indocyanine Green (ICG) (13.7 μM) were also measured under the same conditions.

#### Determination of stability of IT-4 F NPs solution

IT-4 F NPs solution (3.6 μM) was stored in darkness at 4 °C. The absorption spectra and particle size distribution of the solution were measured daily for 7 days.

#### Measurement of temperature increase of IT-4 F NPs solution

IT-4 F NPs solution at different concentrations (12.5 μM, 6.3 μM, 3.1 μM, 1.5 μM, and 0) was irradiated with 735 nm laser (1 W/cm<sup>2</sup>) for 10 min. A thermocouple was then used to record the temperature variation of the solutions.

#### Determination of photothermal cycle of IT-4 F NPs solution

1.0 mL of IT-4 F NPs solution (12.5 μM) was exposed to 735 nm laser (1 W/cm<sup>2</sup>) for 10 min. After the solution was cooled down to room temperature, the irradiation was continued for another 10 min. The temperature of an ICG solution (12.5 μM) was also tested under the same conditions.

#### Determination of photothermal conversion efficiency of IT-4 F NPs

The absorbance at 735 nm of IT-4 F NPs solution was adjusted to 0.1. The solution was exposed to 735 nm laser (1 W/cm<sup>2</sup>) for 10 min and then cooled down for 10 min.

The temperature of pure water was also determined under the same conditions.

#### Cell culture

4T1 cells, a mouse breast cancer cell line, were cultured in an RPMI 1640 medium containing 10% fetal bovine serum. The cells were incubated in an incubator saturated with 5% CO<sub>2</sub> at 37 °C. The cells were digested with 0.25% trypsin-EDTA solution and subjected to subsequent passage.

#### Cytotoxicity assay

**Dark toxicity:** The cytotoxicity of IT-4F NPs on 4T1 cells was determined using the MTT assay. Cells were inoculated into two 96-well plates at a density of  $2 \times 10^4$  cells per well, and incubated for 24 h. Next, the cells were cultured with different concentrations of IT-4F NPs in the dark for 20 h. Then, 200 μL of RPMI 1640 medium containing 0.5% MTT was added to each well, and the cells were cultured for another 4 h. After removing the culture medium, 150 μL of dimethyl sulfoxide (DMSO) was added to each well. The culture plates were then oscillated on a shaker at a low speed for 10 min. The absorption at 490 nm was measured using an enzyme-labeled instrument.

**Phototoxicity:** After incubating with IT-4 F NPs in the dark for 4 h, cells were irradiated with 735 nm laser (1 W/cm<sup>2</sup>) for 10 min. Next, the cells were incubated for 16 h. The remaining steps were the same as those described for the dark toxicity test.

To achieve individual PDT and PTT treatments [22, 23], we maintained a constant temperature (25 °C) or treated the cells with 100 μM ascorbic acid. The remaining steps were the same as those described for the phototoxicity test.

#### Intracellular reactive oxygen species (ROS) test

A green fluorescent probe, DCFH-DA, was used to detect the total ROS in cells. A green fluorescent probe, O22, was used to detect the singlet oxygen in cells. A red fluorescent probe, DHE, was used to detect intracellular superoxide anion. The samples were divided into different groups as follows: PBS group, PBS + L group, IT-4 F NPs group, and IT-4 F NPs + L group.

**Total ROS:** 4T1 cells were cultured in a 6-well plate until their density reached 60-70%. Next, an RPMI 1640 medium containing 12.5 μM IT-4 F NPs was added to the plate to co-culture with 4T1 cells for 4 h. Then, the cells were incubated with a diluted DCFH-DA medium for 30 min. Cells in the PBS + L group and IT-4 F NPs + L group were irradiated with 735 nm laser (1 W/cm<sup>2</sup>) for 10 min. Finally, the cells were observed under an inverted fluorescence microscope, and images were captured.

**Singlet oxygen:** 4T1 cells were cultured in confocal dishes until the density reached 60-70%. Next, an RPMI 1640 medium containing 12.5  $\mu\text{M}$  IT-4 F NPs was added to the 4T1 cells and co-cultured for 4 h. Then, the cells were incubated with a medium diluted with O22 for 30 min. Cells in the PBS+L group and IT-4 F NPs+L group were irradiated with 735 nm laser (1  $\text{W}/\text{cm}^2$ ) for 10 min. Finally, a confocal laser scanning microscope was used to observe the cells and capture their images.

**Superoxide anion:** 4T1 cells were cultured in confocal dishes until the density reached 60-70%. Next, an RPMI 1640 medium containing 12.5 $\mu\text{M}$  IT-4 F NPs was co-cultured with 4T1 cells for 4 h. Then, the cells were incubated with a medium diluted with DHE for 30 min. Cells in the PBS+L group and IT-4 F NPs+L group were irradiated with 735 nm laser (1  $\text{W}/\text{cm}^2$ ) for 10 min. Finally, the confocal laser scanning microscope was used to observe the cells and capture their images.

#### **Immunogenic cell death assays**

4T1 cells were seeded in 24-well plates and treated with IT-4 F NPs (12.5  $\mu\text{M}$ ) for 4 h. Cells were then exposed to 735 nm laser (1  $\text{W}/\text{cm}^2$ ) for 10 min, followed by an additional 3 h incubation. After removing the medium, cells were washed three times with PBS and fixed with 500  $\mu\text{L}$  paraformaldehyde for 25 min. They were used in HMGB1 release, CRT exposure, and ATP release experiments respectively.

**HMGB1 release:** Triton X-100 (500  $\mu\text{L}$ ) was added for 5 min to permeabilize the cells, then BSA (500  $\mu\text{L}$ ) was used to block for 1 h. After washing, the cells were incubated with primary antibody overnight at 4  $^{\circ}\text{C}$ . The next day, the primary antibody was removed, and the cells were washed before adding secondary antibody for 1 h at 4  $^{\circ}\text{C}$ . After further washing, DAPI (500  $\mu\text{L}$ ) was added for 10 min in the dark. Finally, cells were imaged under a fluorescence microscope.

**CRT exposure:** The paraformaldehyde was aspirated, and cells were washed with PBS. Then, 500  $\mu\text{L}$  BSA were added for 1 h at room temperature to block. After removing the BSA, cells were washed with PBS, and 500  $\mu\text{L}$  primary antibody was applied overnight at 4  $^{\circ}\text{C}$ . The primary antibody was removed, and cells were washed three times with PBS. Next, 500  $\mu\text{L}$  secondary antibody was added for 1 h at 4  $^{\circ}\text{C}$ . Following the secondary antibody incubation, cells were washed with PBS and stained with 500  $\mu\text{L}$  DAPI for 10 min in the dark. Finally, cells were examined under a fluorescence microscope and images were captured.

**ATP release:** The culture medium from each well was collected for the detection of ATP using an ATP detection kit according to the manufacturer's instruction, respectively.

#### **Western blot analysis**

4T1 cells were seeded in 6-well plates and cultured for 24 h up to about 80% confluence. The experiment was divided into the following four groups: PBS group, PBS+L group, IT-4 F NPs group, and IT-4 F NPs+L group. L presents laser irradiation. Cells were washed twice with PBS and collected using a cell scraper. Then, the cells were digested with RIPA lysate on ice for 30 min, and the protein solution was obtained by centrifugation. Subsequently, the protein concentration was determined by BCA protein assay kit. Finally, standard western blot was performed. Anti-cleaved Caspase 3 antibody (CST), anti-cleaved GSDME antibody (CST), anti-cleaved Caspase 7 (CST), anti-pMLKL (S345) antibody (CST) were applied. Finally, the protein was detected by Bio-Rad.

#### **Biological experiment in vivo**

The animal experiments were approved by the Ethics Committee for Experimental Animal of The First Affiliated Hospital of Hunan Normal University. Six-week-old female BALB/c mice were used in this experiment.

**Establishment of subcutaneous tumor model:** Mice were subcutaneously inoculated with  $1 \times 10^6$  tumor cells. After the tumor size reached about 200  $\text{mm}^3$ , mice were randomly divided into 4 groups (5 mice in each group) as follows: PBS group, PBS+L group, IT-4 F NPs group, and IT-4 F NPs+L groups. L presents laser irradiation. 100  $\mu\text{L}$  of either PBS or IT-4 F NPs (12.5  $\mu\text{M}$ ) were injected into each tumor site. After injection, mice in the PBS+L group and IT-4 F NPs+L group were irradiated with 735 nm laser (1  $\text{W}/\text{cm}^2$ ) for 10 min. After 2 weeks, the mice were euthanized. During the treatment, the weight of each mouse was measured using a balance, the length and width of the tumor were measured using a vernier caliper, and the tumor volume was calculated. At the same time, to calculate the survival rate of mice, BALB/c tumor-bearing mice were randomly divided into 4 treatment groups ( $n=5$  in each group), and the treatment methods were the same as above. The survival rate of mice in different groups was calculated according to the formula of  $N_{\text{live}}/N_{\text{total}}$ , where  $N_{\text{live}}$  is the number of live animals, and  $N_{\text{total}}$  the number of the initial animals before treatment.

#### **Infrared thermal imaging of mouse tumor**

Mice in the PBS+L group and IT-4 F NPs+L group were irradiated with 735 nm laser (1  $\text{W}/\text{cm}^2$ ) for 10 min. During irradiation, a thermal imager was used to take their photos, and the temperature changes of the tumor site in tumor-bearing mice were recorded.

#### **In vivo fluorescence imaging**

When the tumors of BALB/c tumor-bearing mice reached approximately 200  $\text{mm}^3$ , the mice were injected

intratumorally with 100  $\mu\text{L}$  of IT-4 F NPs (12.5  $\mu\text{M}$ ). Subsequently, fluorescence imaging experiments were performed using the VILBER imaging system ( $\lambda_{\text{ex}} = 680 \text{ nm}$ ,  $\lambda_{\text{em}} = 700\text{--}750 \text{ nm}$ ), and draw the contour of the mouse with lines [24].

#### Detection and analysis of delivery detection mechanism

The blood of mice was analyzed by blood biochemistry, blood routine, and cytokine detection. Visceral organs and tumors of mice were sectioned. The partial tumor and spleen were used for immunocyte flow cytometry analysis. The partial tumors were used for multiple fluorescent staining section analysis.

#### Establishing organoids and evaluating the antitumor effect

At the beginning of the experiment, all patients provided informed consent. We obtained tumor biospecimens from patient with breast cancer. The solid tumors were fragmented and embedded in a hydrogel containing cells ( $2 \times 10^5$  cells/mL), then seeded into 48-well plates. On day 5, the organoids were treated, refreshed with new medium, and cultured for an additional 2 days before assessing cell viability.

#### Theoretical calculations

All theoretical calculations are performed on the Gaussian 16, Revision C.01. (Gaussian, Inc., Wallingford CT, 2019). For density-functional theory (DFT) calculations, The HOMO/LUMO orbitals of the monomer and ground-state ( $S_0$ ) molecular geometries are stimulated at B3LYP/6-31G(d) level. The electrostatic potential is then calculated based on the optimized  $S_0$  molecular geometries at the same level and analyzed with Multiwfn 3.8 dev [25, 26]. The HOMO/LUMO orbitals of the Dimer are stimulated using B3LYP-GD3BJ/6-31G(d). For time-dependent DFT (TD-DFT) calculations, molecular geometry optimization in the first singlet excited state ( $S_1$ ), excited energies, and EST are calculated using B3LYP functional, 6-31G(d) basis set. The HOMO/LUMO orbitals and Maps of ESP surfaces are visualized with the Visual Molecular Dynamic program [27].

#### Data analysis

At least three times were repeated for all experiments with error bars (mean  $\pm$  SD). Significance analysis was performed using One-way ANOVA. The significant differences were indicated as follows: \*\*\* $p < 0.001$ , \*\* $p < 0.01$ , and \* $p < 0.05$ . The statistical analysis software application is GraphPad Prism 8.0.2. The number of mouse samples in immune data analysis was 3 ( $n = 3$ ).

## Results and discussion

As shown in Fig. 1A, IT-4 F features a large planar indacenodithienothiophene (IDTT) central unit as an electron-donating fused-ring core, and a fluorinated 2-(3-oxo-2,3-dihydroinden-1-ylidene) malononitrile (INCN) as an electron-withdrawing unit. This A-D-A structure with strong intramolecular charge transfer (ICT) enables NIR absorption and fluorescence.

To understand the photophysical properties of IT-4 F, theoretical calculations at the b3lyp/6-31 g(d) level were carried out using density functional theory (DFT). The electrostatic potential (ESP) map of IT-4 F shown in Fig. 1B revealed that the positively charged regions are concentrated on the benzene and thiophene rings in the center of the molecule, while negative charges are mainly present on its terminal units. As shown in Fig. 1C, the highest occupied molecular orbital (HOMO) orbitals are predominantly distributed on the electron-donating benzene and thiophene core, and to a lesser extent on both ends of the molecule. The energy gap ( $\Delta E$ ) between HOMO and the lower unoccupied molecular orbital (LUMO) of IT-4 F was calculated as 2.093 eV, giving it a long emission wavelength. The energy gap between the excited singlet (S) and excited triplet (T) states ( $\Delta E_{\text{ST}}$ ) was small, with a  $\Delta E_{\text{S1T3}}$  of only 0.062 eV, facilitating the intersystem crossing (ISC) and promoting the generation of singlet oxygen.

To understand the photophysical properties of the molecules in the aggregated state, the HOMO-LUMO orbitals of the IT-4 F dimer were further calculated. As shown in Fig. 1D, the HOMO orbitals are mainly distributed on the two molecules, while the LUMO orbitals are mainly distributed on one of the molecules of the dimer, where strong intermolecular charge transfer enhances the molecular photothermal conversion efficiency. Compared to the monomolecular state, both  $\Delta E$  and  $\Delta E_{\text{ST}}$  are smaller in the aggregated state, extending the absorption/emission wavelength and favoring the generation of singlet oxygen.

As shown in Fig. 1E and F, IT-4 F dissolved in THF displayed NIR absorption and fluorescence peaks at 667 nm and 750 nm, respectively. Furthermore, the hydrophobic IT-4 F was further assembled with the amphiphilic DSPE-PEG-NH<sub>2</sub> to form water-dispersible IT-4 F NPs. Upon formation of the NPs,  $\pi$ - $\pi$  stacking interactions between molecules are enhanced, resulting in a red shift in both absorption and fluorescence spectra to 728 nm and 817 nm, respectively (Fig. 1G, H). The Zeta potential of the aqueous IT-4 F NPs solution was measured at -23.7 mV, indicating good water dispersibility. Furthermore, these NPs demonstrated excellent stability, as evidenced by the consistent absorption spectra, particle distribution, and morphology over a 7-day period (Fig. 1I). As shown in Fig. S1, the PDI of the NPs was found to

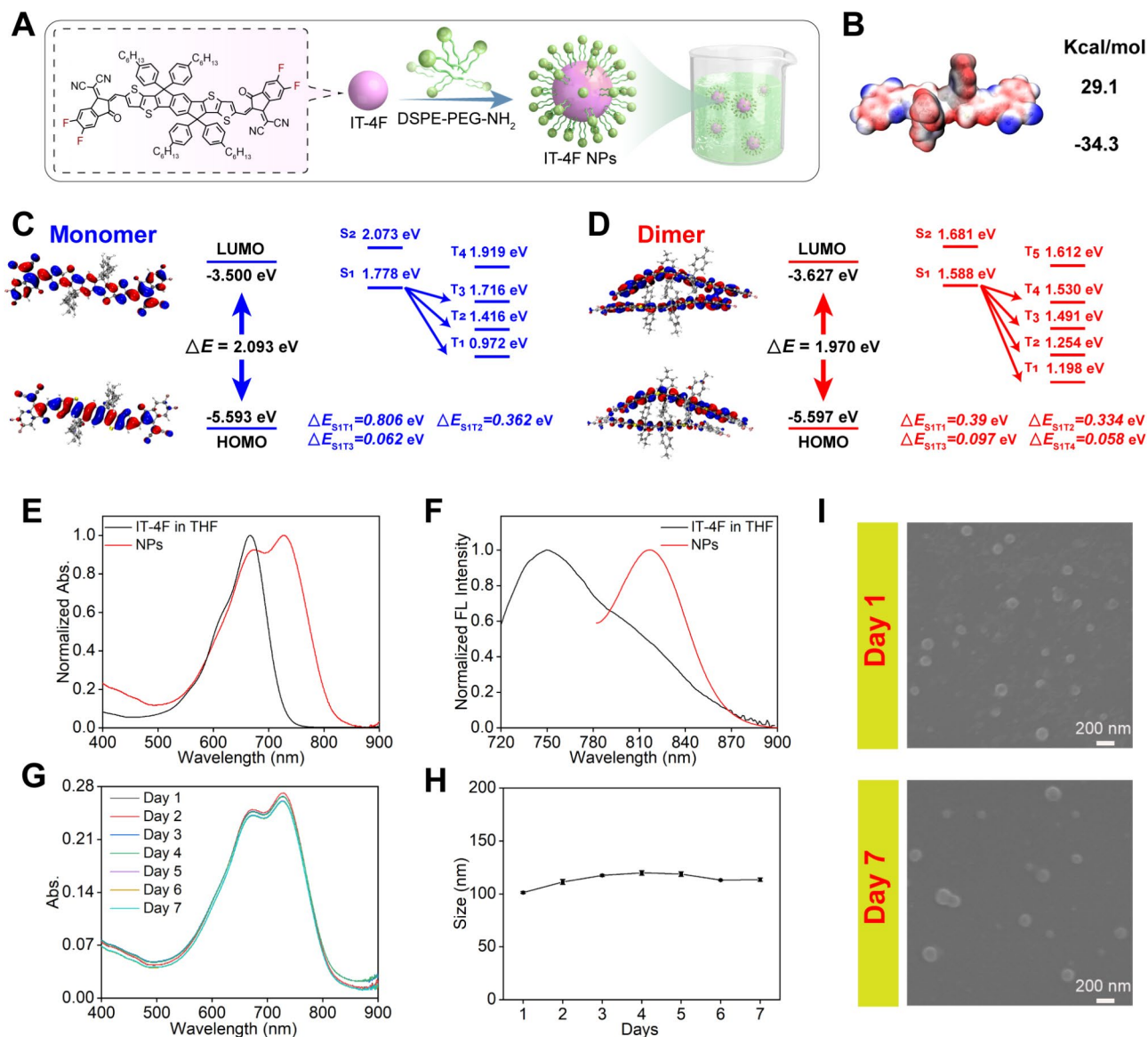


**Fig. 1** (A) Schematic representation showing the preparation of IT-4 F NPs. (B) The ESP map of IT-4 F. (C, D) Diagram showing calculated frontier molecular orbital of monomeric and dimeric IT-4 F NPs. Calculated energy levels of the singlet and triplet excited states of monomeric and dimeric IT-4 F NPs.  $\Delta E = E_{LUMO} - E_{HOMO}$  (E) Ultra-violet-visible (UV-vis) absorption spectra and (F) fluorescence spectra of IT-4 F NPs aqueous solution and IT-4 F in THF. Time-dependent changes of (G) UV-vis absorption and (H) particle distribution of NPs. (I) SEM images of IT-4 F NPs on the 1st and 7th days of preparation

be 0.263, and the average diameter was approximately 103 nm, a size suitable for cellular uptake.

As displayed in Fig. 2A-C, the absorption spectra of IT-4 F NPs showed minimal changes following laser irradiation, whereas the same parameters for Indocyanine Green (ICG) showed a significant decline. Surprisingly, IT-4 F NPs exhibited excellent ROS generation capability under 735 nm laser irradiation. As shown in Fig. 2D-I, laser irradiation of IT-4 F NPs aqueous solution induced the fluorescence of SOSG and DHR123 increased markedly. Conversely, in the absence of IT-4 F NPs, the fluorescence of SOSG and DHR123 showed no obvious changes, suggesting IT-4 F NPs could effectively generate

$^1O_2$  and  $O_2^{\cdot-}$  upon laser irradiation. The  $^1O_2$  generation quantum yield was calculated to be 31.5%.

Due to the strong NIR absorption, IT-4 F NPs exhibited significant photothermal conversion capability. As shown in Fig. 2J, under 735 nm laser irradiation, the temperature of the IT-4 F NPs solution increased with both higher concentrations and longer irradiation times. For instance, a 12.5  $\mu$ M IT-4 F NPs solution reached approximately 55 °C, whereas pure water (without NPs) showed only a 4 °C increase after 10 min of irradiation at 1 W/cm<sup>2</sup> (Fig. 2K). The PCE of the NPs at 735 nm was calculated to be 42.8%. In addition, the NPs exhibited excellent photostability. Similarly, the temperature of the NPs

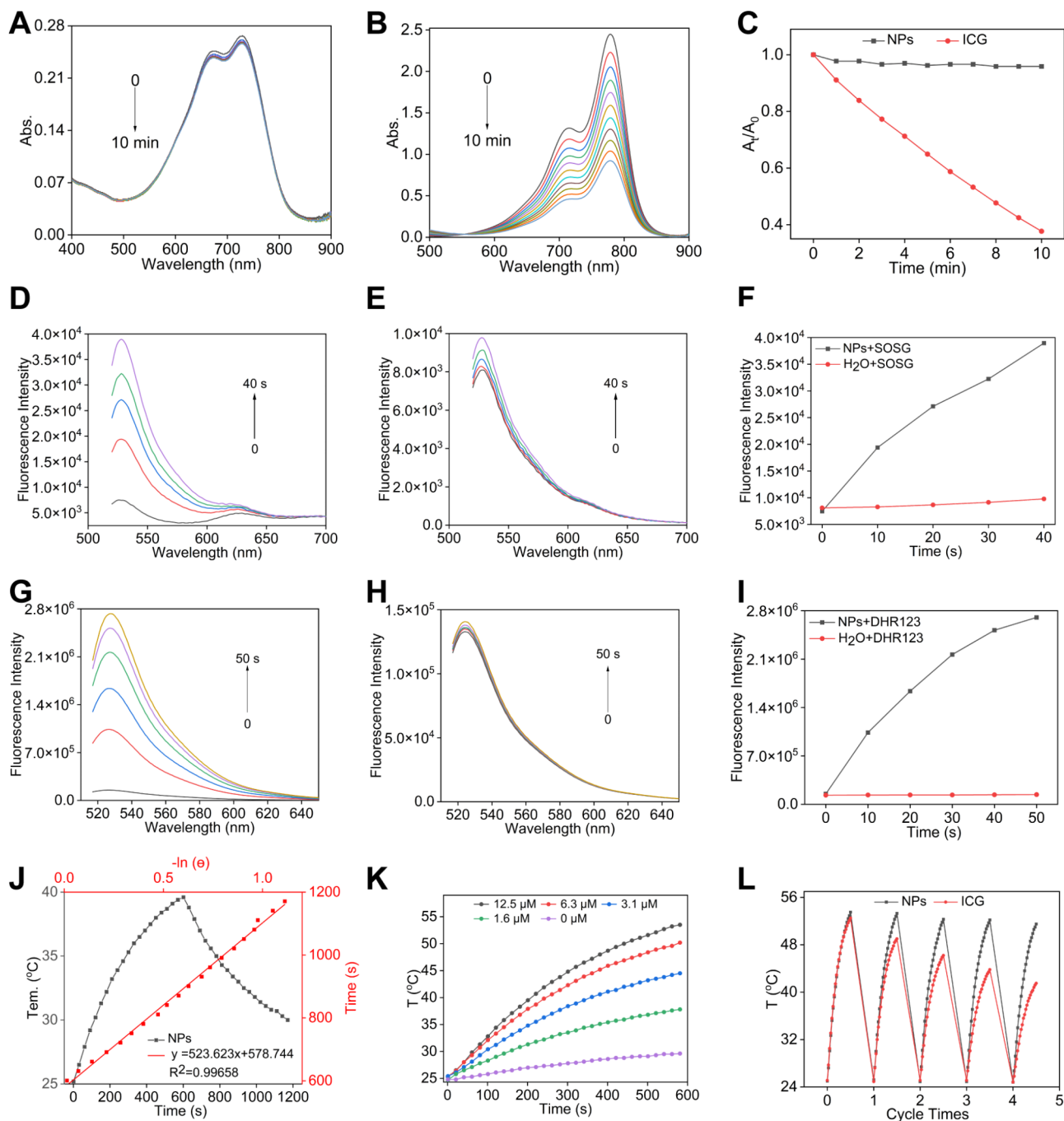


**Fig. 2** The change in the UV-Vis absorption spectrum of IT-4 F NPs (A) and ICG (B) under 735 nm laser irradiation at  $0.5 \text{ W}/\text{cm}^2$  for 10 min. (C) Time-dependent changes of normalized absorbance at 728 nm of IT-4 F NPs and those at 779 nm of ICG. UV-vis absorption spectral change of SOSG in the (D) presence and (E) absence of 5  $\mu\text{M}$  IT-4 F NPs after being exposed to 735 nm laser irradiation. (F) Changes of the corresponding absorbance ratio ( $A_t/A_0$ ) at 378 nm of SOSG in the (G) presence and (H) absence of 5  $\mu\text{M}$  IT-4 F NPs after being exposed to 735 nm laser irradiation. (I) Changes of the corresponding fluorescent intensity at 529 nm of DHR123. (J) Photothermal conversion efficiency of IT-4 F NPs. (K) Time-dependent temperature changes of IT-4 F NPs at different concentrations after irradiation. (L) Temperature variations of IT-4 F NPs or ICG irradiated with 735 nm laser ( $1 \text{ W}/\text{cm}^2$ ) for 5 cycles

solution exposed to laser irradiation could reach to  $55^\circ\text{C}$  after 5 laser on-off cycles, while that of ICG solution only increased to  $42^\circ\text{C}$  (Fig. 2L).

Figure 3A shows the schematic application of IT-4 F NPs in in vitro cell experiments. The cytotoxicity and phototoxicity of IT-4 F NPs against 4T1 cells were quantitatively evaluated. To achieve individual PDT and

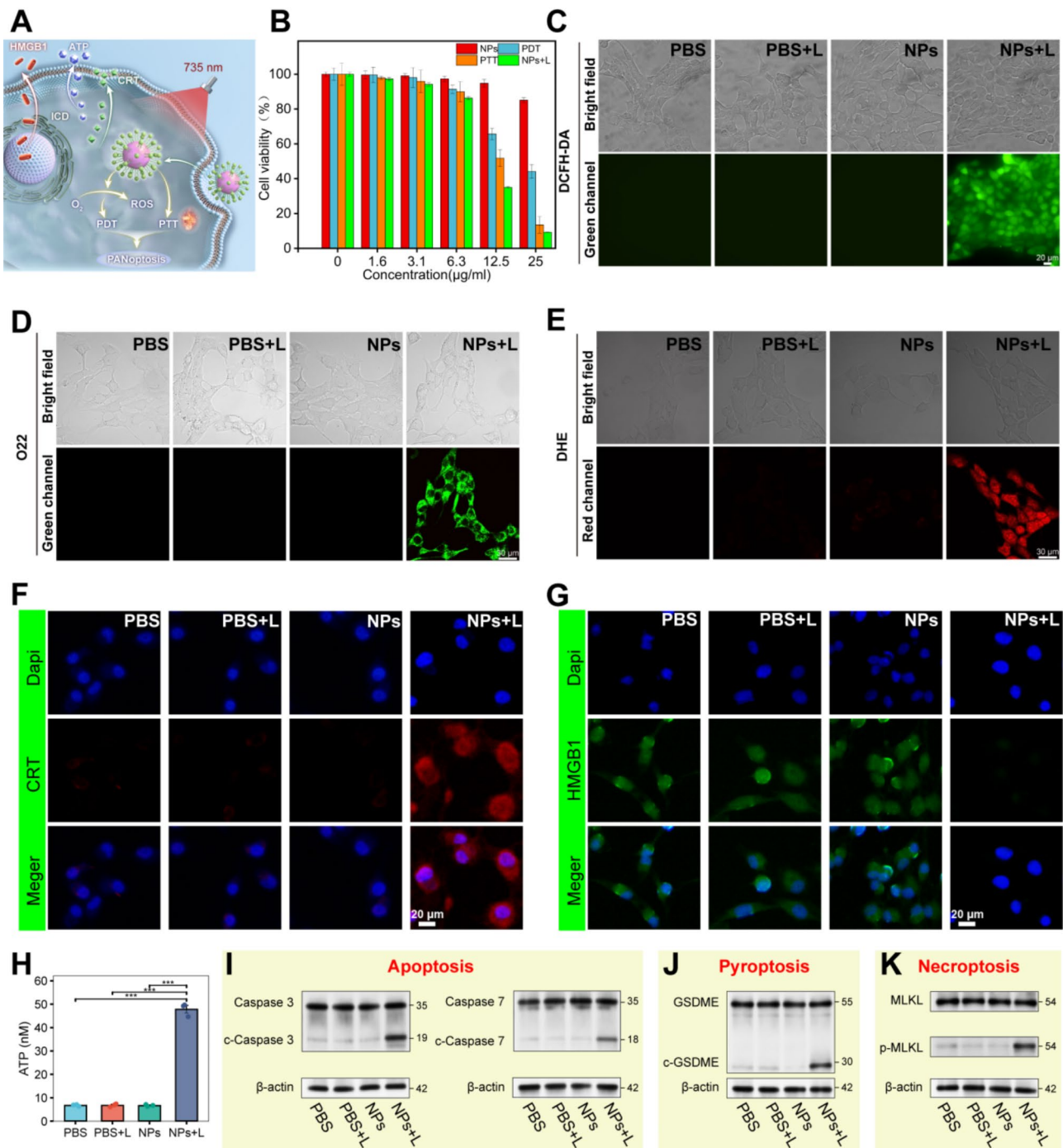


**Fig. 3** (A) Schematic diagram of the in vitro cell experiment application of IT-4 F NPs. (B) Quantitative detection of 4T1 cells viability following PDT, PTT and simultaneous PDT/PTT. Bright field and fluorescent images of 4T1 cells incubated with different treatments in the presence of (C) DCFH-DA, (D) O22, and (E) DHE. Fluorescent images of CRT (F) exposure and HMGB1 (G) release in 4T1 cells. (H) Extracellular secretion of ATP from 4T1 cells before and after different treatments ( $n=3$ , Data are presented as the mean  $\pm$  s.e.m. Statistical analysis was performed using two-way ANOVA. Significance levels are indicated as  $*p < 0.05$ ,  $**p < 0.01$ , and  $***p < 0.001$ ). PANoptosis induced by IT-4 F NPs + L treatment. Western blot analysis of cleaved Caspase 3, cleaved Caspase 7 (I), cleaved GSDME (J), pMLKL (K) in 4T1 cells after varied treatments

PTT treatments, we maintained a constant temperature (25 °C) or treated the cells with 100  $\mu\text{M}$  ascorbic acid, a well-known ROS scavenger. The MTT assay was used to quantitatively evaluate the effect of IT-4 F NPs on 4T1 cells. As shown in Fig. 3B, in the absence of laser irradiation, cell viability remained above 94% after incubation with 12.5  $\mu\text{M}$  IT-4 F NPs. However, when cells were treated with the same concentration of NPs followed by 735 nm laser irradiation for 10 min, individual PDT and PTT treatments resulted in 35% and 49% cell death, respectively. When PDT and PTT were performed simultaneously, cell viability decreased to approximately 35%. Furthermore, cell viability following laser exposure was found to be concentration-dependent. These results suggest that either IT-4 F NPs or laser irradiation alone do not induce significant cancer cell death, while their combination leads to a substantial reduction in cell viability. This demonstrates their potential for synergistic phototherapy. To investigate whether IT-4 F NPs induce toxicity in normal tissues, we conducted additional experiments using different doses of IT-4 F NPs on the normal murine mammary epithelial cell line NMuMG. As shown in Fig. S4, combined with the results of IT-4 F NPs treatment on 4T1 cells, 12.5  $\mu\text{M}$  IT-4 F NPs effectively killed tumor cells while having minimal impact on normal cells.

To further explore the intracellular ROS generation, live cells were incubated with IT-4 F NPs and various ROS probes: DCFH-DA, O22, and DHE, which are indicative of general ROS,  $^1\text{O}_2$ , and superoxide anions, respectively. Following 735 nm laser irradiation at 1 W/cm<sup>2</sup> for 10 min, cells co-incubated with IT-4 F NPs (12.5  $\mu\text{M}$ ) and DCFH-DA exhibited strong green fluorescence (Fig. 3C), indicative of robust ROS production. Similarly, cells treated with IT-4 F NPs (12.5  $\mu\text{M}$ ) and O22 showed significant green fluorescence after the same irradiation conditions (Fig. 3D), confirming the generation of  $^1\text{O}_2$ . Additionally, cells co-incubated with IT-4 F NPs and DHR123 displayed strong red fluorescence under the same laser exposure (Fig. 3E). In contrast, no notable fluorescence was observed in the dark or in the absence of IT-4 F NPs, further supporting that IT-4 F NPs can efficiently enter cells and generate both  $^1\text{O}_2$  and superoxide anions upon laser irradiation. Additionally, IT-4 F NPs can effectively generate ROS even in a hypoxic environment and still kill tumor cells, making them a promising candidate for PDT in solid tumors (Figs. S2 and S3).

Since laser irradiation induces tumor cell ICD leading to the expression of damage-associated molecular patterns (DAMPs), the ICD effect mediated by IT-4 F NPs was investigated. Key indicators were examined, including CRT expression on the cell surface and the release of ATP and HMGB-1 from treated cancer cells. DAMPs released during ICD function as tumor-associated

antigens. Its recognized by receptors on DC cell surfaces to enable antigen presentation. Consequently, an inverted fluorescence microscope was used to examine CRT, HMGB1, and ATP. In 4T1 cells, CRT expression was minimal under treatments with PBS, PBS+L, or IT-4 F NPs alone. However, IT-4 F NPs combined with laser irradiation significantly increased CRT exposure on the cell surface, along with substantial HMGB1 and ATP release (Fig. 3F-H). This promotes the phagocytosis of apoptotic cancer cells by DCs, enhancing the antitumor immune response. In summary, IT-4 F NPs combined with laser irradiation effectively induce the ICD effect in cancer cells.

PANoptosis is generally considered to be an inflammatory PCD regulated by the PANoptosome complex, which is characterized by activation of pyroptotic, apoptotic and necroptotic pathways [28]. Caspase 3 and Caspase 7, essential proteins in the apoptosis pathway, are known to be activated during the early stage of apoptosis. The up-regulation of cleaved Caspase 3/7 expression, as depicted in Fig. 3I, signifies the activation of cleaved Caspase 3/7 within the IT-4 F NPs with illumination group, thus providing additional confirmation of apoptosis occurrence. Furthermore, considering that pyroptosis represents another significant mechanism of ROS induction, we investigated the expression of associated proteins [29]. The up-regulation of cleaved GSDME expression can be observed in the IT-4 F NPs with illumination group (Fig. 3J), confirming the activation of cleaved GSDME. Besides apoptosis and pyroptosis, previous studies have demonstrated that ROS can induce necrotic apoptosis, specifically MLKL phosphorylation [30]. Compared with PBS, PBS with illumination and IT-4 F NPs group, the expression of pMLKL in IT-4 F NPs with illumination group was significantly up-regulated, which confirmed the occurrence of necroptosis (Fig. 3K). These findings indicate that IT-4 F NPs + laser treatment induces apoptosis through caspase3/7 activation, while also triggering pyroptosis via GSDME cleavage and necroptosis via MLKL phosphorylation. ROS generated by IT-4 F NPs under laser irradiation are central to the induction of PANoptosis, IT-4 F NPs induce ROS generation, which triggers the activation of multiple cell death pathways. For example, ROS-mediated activation of caspase3/7 leads to apoptosis, GSDME activation triggers pyroptosis, and MLKL activation causes necroptosis. These pathways are interconnected and promote the inflammatory response, further enhancing the immune system's ability to target tumor cells [31].

Figure 4A shows the treatment scheme of anti-tumor therapy in vivo. The imaging capabilities of IT-4 F NPs in 4T1 tumor-bearing mice were evaluated by intratumoral injection of an aqueous solution of IT-4 F NPs. Following injection, the tumor site displayed strong NIR

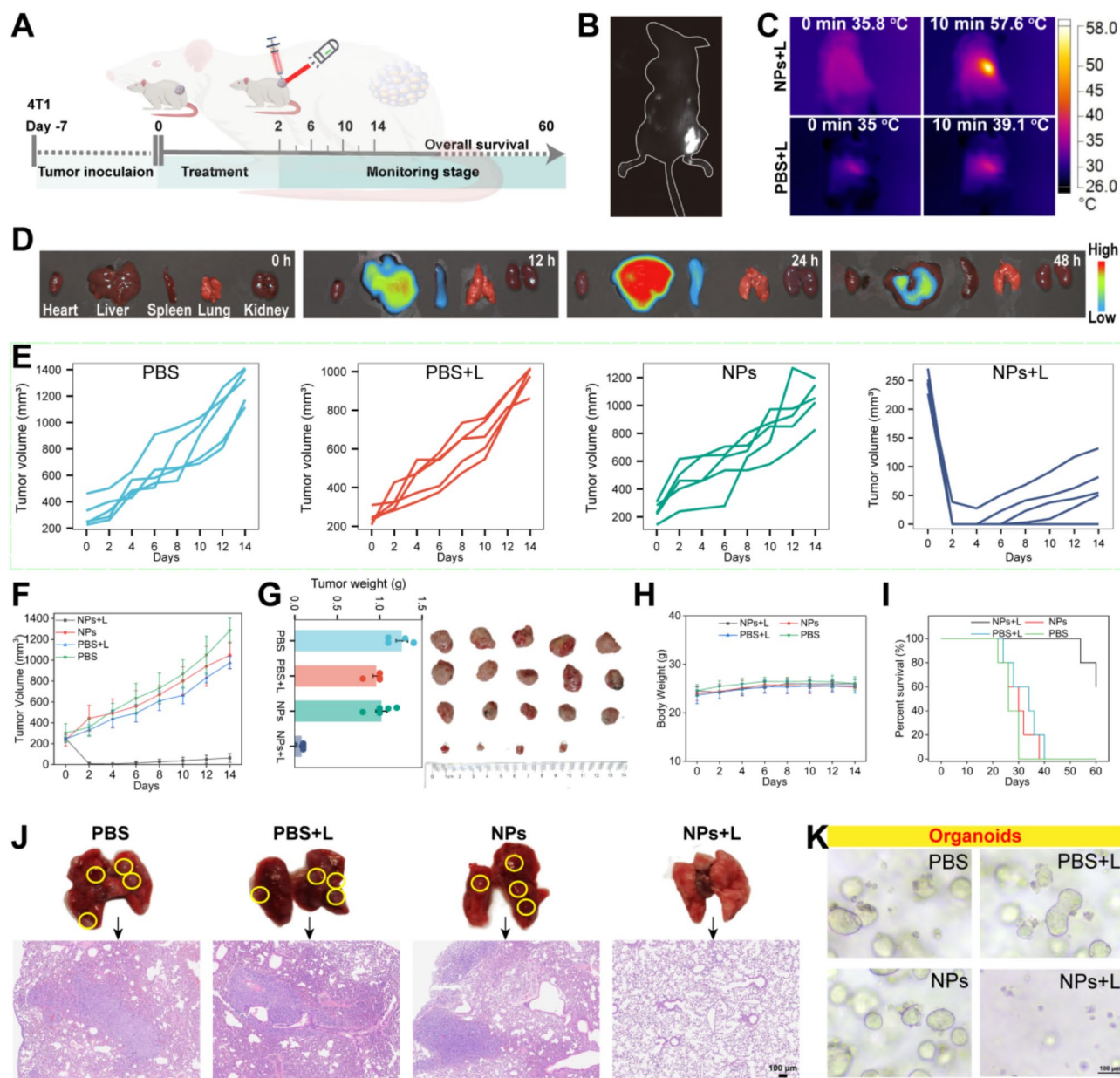


**Fig. 4** (A) Treatment schedule of in vivo antitumor therapy. (B) NIR fluorescence image and (C) photothermal images of 4T1 tumor-bearing mice injected with IT-4 F NPs. (D) NIR fluorescence images of major organs at different time intervals after IT-4 F NPs injection. Time-dependent changes of tumor volume (E and F), tumor images and tumor weight (G) and body weight (H) of mice in different groups. (I) Survival rate after various treatments. (J) Representative images showing that mice in the IT-4 F NPs + L treatment group had fewer lung metastases, and H&E staining images of lung tissue (where circles indicate metastatic tumors). (K) Microscopic images of organoids following different treatment conditions

fluorescence, confirming the successful localization of the NPs (Fig. 4B). Furthermore, after the injection of IT-4 F NPs, the tumor site was irradiated with 735 nm laser ( $1 \text{ W/cm}^2$ ) for 10 min, resulting in a temperature increase to approximately  $57.6 \text{ }^\circ\text{C}$ , which is sufficient to induce tumor cell ablation. In contrast, in the absence of IT-4 F NPs, the temperature at the laser-irradiated site increased by only  $4 \text{ }^\circ\text{C}$  (Fig. 4C), demonstrating the excellent in vivo fluorescence and photothermal imaging capabilities of the NPs. Additionally, we conducted biodistribution and

clearance studies. As shown in Fig. 4D, the nanoparticles mainly accumulate in the liver and spleen, with relatively low accumulation in other organs.

The phototherapeutic effects of IT-4 F NPs were also investigated in tumor-bearing mice. The mice were randomly assigned to one of four groups: saline, saline + L, IT-4 F NPs, and IT-4 F NPs + L. Tumor growth in the IT-4 F NPs + L group showed a significant reduction compared to the other groups, where tumor growth remained similar (Fig. 4E-G). Importantly, there were no significant

differences in body weight among the four groups (Fig. 4H), indicating that the treatments caused minimal systemic toxicity. Survival analysis further revealed that 60% of the tumor-bearing mice in the IT-4 F NPs+L group survived for more than 60 days, while all mice in the saline, saline+L, and IT-4 F NPs groups had died by day 40 (Fig. 4I). Metastasis analysis revealed numerous metastatic tumors in the lungs of mice from the saline, saline+L, and IT-4 F NPs groups. In contrast, no metastatic lesions were observed in the lungs of mice treated with IT-4 F NPs+L (Fig. 4J), providing further evidence that the combination of IT-4 F NPs and laser irradiation can prevent tumor metastasis. Moreover, IT-4 F NPs with illumination can have considerable antitumor effect in patient-derived organoids (Fig. 4K).

The tumors were excised and analyzed using H&E staining, Ki67, and TUNEL assays to assess tissue damage, cell proliferation, and apoptosis. H&E staining revealed a distinct necrotic region in the tumors from the NPs+L group (Fig. 5A). Ki67 analysis indicated a significant reduction in tumor cell proliferation in this group (Fig. 5B). Furthermore, TUNEL staining showed

prominent green fluorescence in the NPs+L group, indicating enhanced apoptosis (Fig. 5C). These results suggest that IT-4 F NPs, when combined with laser treatment, effectively induce tumor cell death and inhibit tumor growth.

To evaluate the biocompatibility of IT-4 F NPs, blood routine and blood biochemistry analyses were performed, with focus on liver, kidney, and heart functions. As shown in Fig. 5D-F, neither IT-4 F NPs alone nor IT-4 F NPs+L treatment caused significant adverse effects on the mice. Additionally, H&E staining of major organs confirmed the excellent biocompatibility of IT-4 F NPs, with no observable tissue damage.

We quantified the expression of TNF- $\alpha$ , IFN- $\gamma$ , IL-6 and IL-10 in serum. As depicted in Fig. 6A, the results suggest that IT-4 F NPs+L can efficiently help induce tumor cell apoptosis, inhibit tumor growth, and enhance immune response. Subsequently, the anti-tumor immunity mechanism induced by IT-4 F NPs with illumination was investigated via flow cytometry and multiple fluorescent staining section analysis. As shown in Fig. 6B-C, to analyze the in vivo TME, flow cytometry was conducted

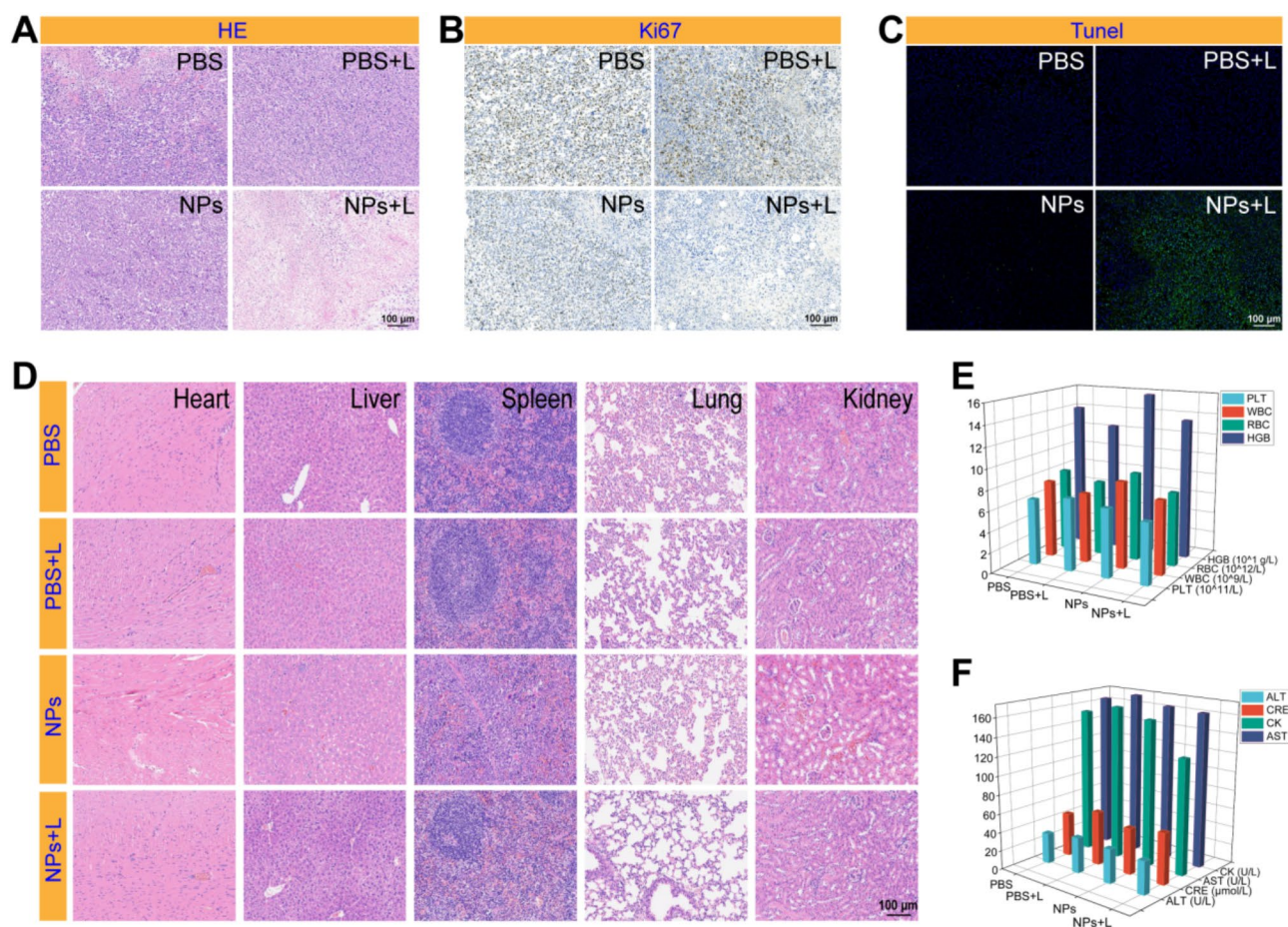


**Fig. 5** H&E (A), Ki67 (B), and TUNEL (C) analyses of tumors in different groups. (D) H&E staining of major organs of mice in different groups. Blood routine analysis (E) and blood biochemistry (F) analysis of mice in different groups

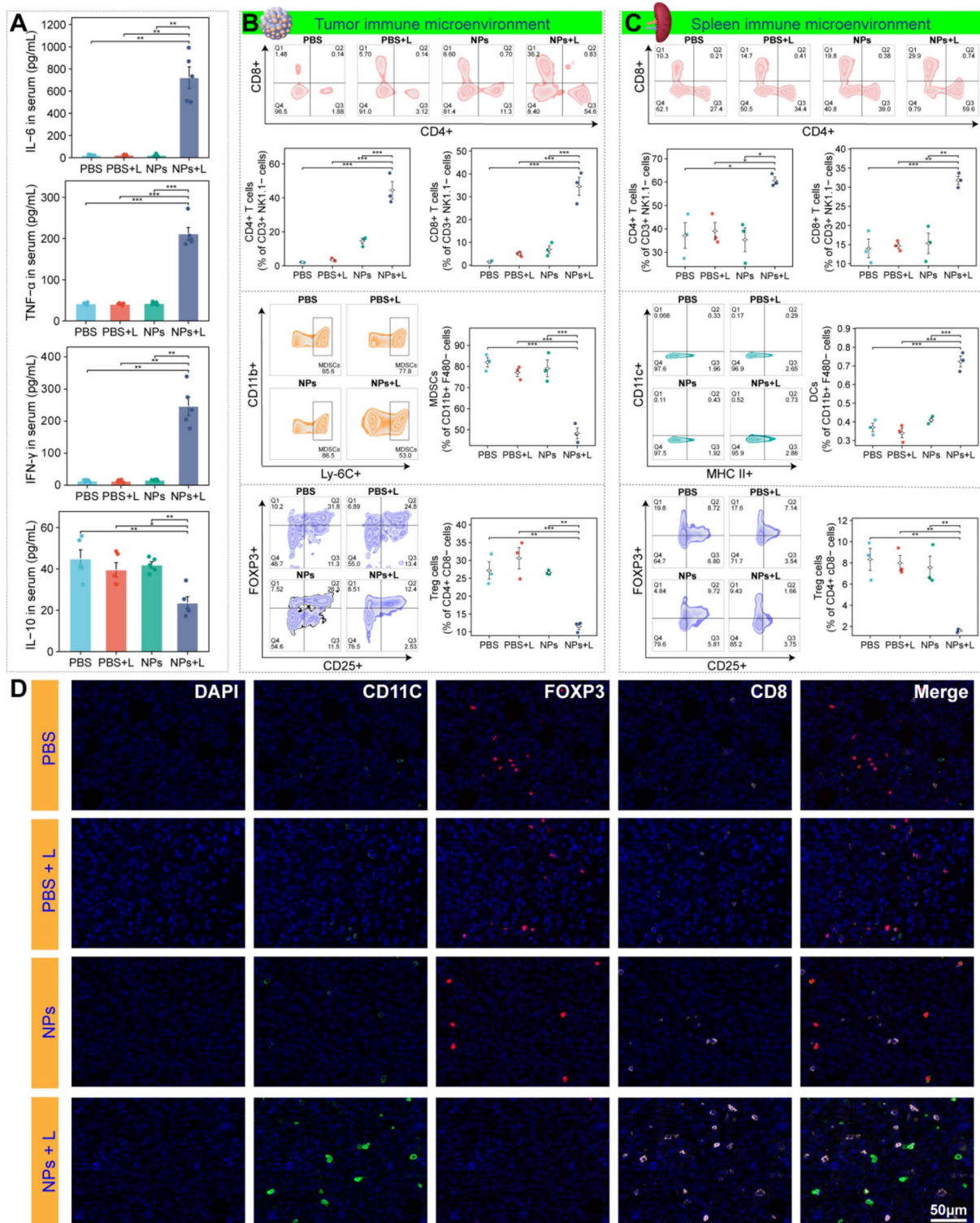


**Fig. 6** (A) Serum cytokines analysis of mice in the four treatment groups (n=5, Data are presented as the mean ± s.e.m. Statistical analysis was performed using two-way ANOVA. Significance levels are indicated as \*p < 0.05, \*\*p < 0.01, and \*\*\*p < 0.001). (B) Comparison of tumor immune microenvironment in mice after different treatments (n=3). (C) Comparison of spleen immune microenvironment in mice after different treatments (n=3). (D) Multiplex fluorescence staining analysis of tumor sections in mice after different treatments

on disaggregated tumor and spleen cells from mice treated with the four treatment groups. Flow cytometry analysis revealed that the proportion of CD8<sup>+</sup> T cells and CD4<sup>+</sup> T cells in the tumor microenvironment increased from 1.51% to 2.11% (PBS) to 34.5% and 44.47% (IT-4 F NPs + laser), while the infiltration proportion of MDSCs and Treg decreased by 33.7% and 15.69%. The proportion of CD8<sup>+</sup> T cells and CD4<sup>+</sup> T cells in the spleen increased from 14.03% to 37.17% (PBS) to 31.8% and 60.6% (IT-4 F NPs + laser), respectively. Additionally, the proportion of DC cells increased by 0.35%, while the infiltration of Treg cells decreased by 6.72%. The percentage infiltration of CD8<sup>+</sup>/CD4<sup>+</sup> T of the tumor and spleen was significantly increased after IT-4 F NPs + L treatment, indicating the capability of IT-4 F NPs + L treatment to elicit an adaptive immune response mediated by CD4<sup>+</sup> and CD8<sup>+</sup> T cells. In addition, the population of myeloid-derived suppressor cells (MDSCs) and Treg cells of the tumor in the IT-4 F NPs + L group was significantly decreased compared with the other treatment groups. Besides, more mature DC cells and less suppressive Treg cells were recruited in the spleen after IT-4 F NPs + L compared with that of mice treated with the saline, saline + L, and IT-4 F NPs groups. When DC cells (which play a crucial role in the immune response) recognize an antigen, MHC-I molecules display it on their surface. Upon migrating to lymph nodes, DCs present the antigen to T cells, triggering cellular immunity. At the same time, we also verified the increase of CD8<sup>+</sup> T cells, CD4<sup>+</sup> T cells and the decrease of Treg cells by immunofluorescence analysis of tumors (Fig. 6D). In summary, these results indicate that IT-4 F NPs + L can effectively enhance the tumor-specific immune response.

## Conclusion

This study developed A-D-A type phototherapeutics based on IT-4 F molecule for tumor immuno-phototherapy. These IT-4 F NPs exhibit excellent NIR absorption and fluorescence properties, enabling the simultaneous generation of ROS and heat under single-wavelength laser excitation at 735 nm. They achieved a high PCE of 42.8% with outstanding photostability and biocompatibility. In tumor, IT-4 F NPs through the combination of PTT and PDT effectively induced ICD and PANoptosis in tumor cells. This included increased infiltration of CD8<sup>+</sup> and CD4<sup>+</sup> T cells and reduced proportions of immunosuppressive cells such as MDSCs and Tregs. Additionally, IT-4 F NPs demonstrated significant anti-tumor effects in patient-derived organoid models. In conclusion, IT-4 F NPs offer a highly efficient, safe, and promising new strategy for cancer treatment by integrating the advantages of PTT, PDT, and IPTT. This study provides important theoretical and practical support for advancing cancer immuno-photodynamic therapy.

## Supplementary Information

The online version contains supplementary material available at <https://doi.org/10.1186/s12951-025-03381-3>.

Supplementary Material 1

Supplementary Material 2

Supplementary Material 3

Supplementary Material 4

Supplementary Material 5

## Acknowledgements

This work was supported by the National Natural Science Foundation of China (Nos. 62375289 and 62175262); The Natural Science Foundation of Hunan Province (Nos. 2024JJ9285); The Scientific Research Project of Hunan Provincial Department of Education (Nos. 22B0081).

## Author contributions

Jianing Yi: Funding acquisition and supervision. Minhuan Lan: Funding acquisition and supervision. Jie Zeng: Supervision. E Pang and Yuanyu Tang: Conceptualization, investigation, and writing of the original draft. Shaojing Zhao and Wenjie Gao: Methodology, formal analysis, and writing of the original draft. Yangtian Ye: Original manuscript writing, reviewing, formal analysis, and editing. Jie Yu and Pan Zhu: Investigation, methodology.

## Data availability

No datasets were generated or analysed during the current study.

## Declarations

### Ethical approval

Animal experiments were approved by the First Affiliated Hospital of Hunan Normal University (No. 2024-146). The human breast cancer tissues received approved from the Clinical Ethics Committee of Sir Run Run Hospital of Nanjing Medical University, and adhered to the research principles outlined in the Declaration of Helsinki (No. 2024-SR-037).

### Competing interests

The authors declare no competing interests.

### Author details

<sup>1</sup>Department of Breast and Thyroid Gland Surgery, Hunan Provincial Maternal And Child Health Care Hospital, Changsha, Hunan 410008, China

<sup>2</sup>College of Chemistry and Chemical Engineering, Central South University, Changsha, Hunan 410083, China

<sup>3</sup>Department of General Surgery, Sir Run Run Hospital of Nanjing Medical University, Nanjing, Jiangsu 211166, China

<sup>4</sup>Department of Breast and Thyroid Gland Surgery, Hunan Provincial People's Hospital, The First Affiliated Hospital of Hunan Normal University, Changsha, Hunan 410005, China

Received: 24 January 2025 / Accepted: 9 April 2025

Published online: 23 April 2025

## References

- Lu Y, Sun W, Du J, Fan J, Peng X. Immuno-photodynamic therapy (IPDT): organic photosensitizers and their application in Cancer ablation. *JACS Au*. 2023;3:682–99.
- An J, Lv KP, Chau CV, Lim JH, Parida R, Huang X, Debnath S, Xu Y, Zheng S, Sedgwick AC, Lee JY, Luo D, Liu Q, Sessler JL, Kim JS. Lutetium Texaphyrin-Celecoxib conjugate as a potential Immuno-Photodynamic therapy agent. *J Am Chem Soc*. 2024;146:19434–48.
- Li C, Liu Z, Cheng Z, Gu S, Zhao W, Zhang Q, Feng Z. Cytokine-induced killer cells-mediated Chlorin e6-loaded gold nanostars for targeted NIR imaging

- and immuno-photodynamic combination therapy for lung cancer. *Biomed Mater.* 2024;19:4.
4. Qu C, Yuan H, Tian M, Zhang X, Xia P, Shi G, Hou R, Li J, Jiang H, Yang Z, Chen T, Li Z, Wang J, Yuan Y. Precise photodynamic therapy by midkine Nanobody-Engineered nanoparticles remodels the microenvironment of pancreatic ductal adenocarcinoma and potentiates the immunotherapy. *ACS Nano.* 2024;18:4019–37.
  5. Ren Q, Wang H, Li D, Dao A, Luo J, Wang D, Zhang P, Huang H. An Electron Donor-Acceptor structured Rhenium(II) complex Photo-Sensitizer evokes mutually reinforcing Closed-Loop ferroptosis and immunotherapy. *Adv Healthc Mater.* 2024;13:e2304067.
  6. Sharma A, Verwilt P, Li M, Ma D, Singh N, Yoo J, Kim Y, Yang Y, Zhu JH, Huang H, Hu XL, He XP, Zeng L, James TD, Peng X, Sessler JL, Kim JS. Theranostic Fluorescent Probes *Chem Rev.* 2024;124:2699–804.
  7. Yuan X, Zhou J, Yuan L, Fan J, Yoon J, Zhang X, Peng X, Tan W. Phototherapy: progress, challenges, and opportunities. *Sci China Chem.* 2025;68:826–65.
  8. Infantino V, Santarsiero A, Convertini P, Todisco S, Iacobazzi V. Cancer cell metabolism in hypoxia: role of HIF-1 as key regulator and therapeutic target. *Int J Mol Sci.* 2021;22:5703.
  9. Chen Z, Han F, Du Y, Shi H, Zhou W. Hypoxic microenvironment in cancer: molecular mechanisms and therapeutic interventions. *Sig Transduct Target Ther.* 2023;8:70.
  10. Wang C, Yuan F, Yan Z, Zhang T, Fu C, Li Y, Dai G, Kim HS, Xia S, Yu L, Debnath S, Ren WX, Shu J, Qiu M, Kim JS. High entropy 2D layered double hydroxide nanosheet toward cascaded nanozyme-Initiated chemodynamic and immune synergistic therapy. *J Am Chem Soc.* 2025;147:136–48.
  11. Huang L, Zhao S, Wu J, Yu L, Singh N, Yang K, Lan M, Wang P, Kim JS. Photodynamic therapy for hypoxic tumors: advances and perspectives-ScienceDirect. *Coord Chem Rev.* 2021;438:213888.
  12. Li J, Yi H, Fu Y, Zhuang J, Zhan Z, Guo L, Zheng J, Yu X, Zhang D. Biodegradable iridium coordinated nanodrugs potentiate photodynamic therapy and immunotherapy of lung cancer. *J Colloid Interface Sci.* 2025;680:9–24.
  13. Lan G, Ni K, Xu Z, Veroneau SS, Song Y, Lin W. Nanoscale Metal-Organic framework overcomes hypoxia for photodynamic therapy primed Cancer immunotherapy. *J Am Chem Soc.* 2018;140:5670–3.
  14. Xing X, Zhu P, Pang E, Zhao S, Tang Y, Hu Z, Ouyang Q, Lan M. D-A-D-structured boron-dipyrromethene with aggregation-induced enhanced phototherapeutic efficiency for near-infrared fluorescent and photoacoustic imaging-guided synergistic photodynamic and photothermal cancer therapy. *Chin Chem Lett.* 2024;35:109452.
  15. Tang Y, Pan T, Pang E, Zhao S, Shen X, Tan Q, Zhu P, He D, Wang B, Song X, Lan M. Thienothiophene-Benzopyran derivative and AQ4N-Assembled liposomes for Near-Infrared II fluorescence Imaging-Guided phototherapy, chemotherapy, and immune activation. *Small.* 2024;e2407680.
  16. Li Y, Du Z, Zhang Y, Kang X, Song J, Chen X, Hu Y, Yang Z, Qi J, Shen X. Boosting theranostic performance of AIEgens using nanocatalyzer for robust Cancer immunotherapy. *Adv Funct Mater.* 2024;34:2315127.
  17. Wu F, Chen H, Li Q, Liu R, Suo Y, Li B, Kong X, Cheng Z, Liu H, Chang Y. Amplifying oxidative stress utilizing multiband luminescence of lanthanide nanoparticles for eliciting systemic antitumor immunity. *Chem Eng J.* 2023;468:12.
  18. Song S, Zhao Y, Kang M, Zhang F, Wu Q, Niu N, Yang H, Wen H, Fu S, Li X, Zhang Z, Tang BZ, Wang D. An NIR-II excitable AIE small molecule with multimodal phototheranostic features for orthotopic breast Cancer treatment. *Adv Mater.* 2024;36:e2309748.
  19. Gui Y, Wang Y, Wang D, Qin Y, Song G, Yan D, Tang BZ, Wang D. Thiophene  $\pi$ -Bridge manipulation of NIR-II AIEgens for multimodal tumor phototheranostics. *Angew Chem Int Edit.* 2024;63:e202318609.
  20. Tsang CY, Zhang Y. Nanomaterials for light-mediated therapeutics in deep tissue. *Chem Soc Rev.* 2024;53:2898–931.
  21. Lee KW, Wan Y, Huang Z, Zhao Q, Li S, Lee CS. Organic optoelectronic materials: A rising star of bioimaging and phototherapy. *Adv Mater.* 2024;36:2306492.
  22. Sheng Z, Hu D, Zheng M, Zhao P, Liu H, Gao D, Gong P, Gao G, Zhang P, Ma Y, Cai L. Smart human serum albumin-indocyanine green nanoparticles generated by programmed assembly for dual-modal imaging-guided cancer synergistic phototherapy. *ACS Nano.* 2014;8:12310–22.
  23. Hu D, Sheng Z, Gao G, Siu F, Liu C, Wan Q, Gong P, Zheng H, Ma Y, Cai L. Activatable albumin-photosensitizer nanoassemblies for triple-modal imaging and thermal-modulated photodynamic therapy of cancer. *Biomaterials.* 2016;93:10–9.
  24. Sheng Z, Guo B, Hu D, Xu S, Wu W, Liew WH, Yao K, Jiang J, Liu C, Zheng H, Liu B. Bright Aggregation-Induced-Emission Dots for targeted synergetic NIR-II fluorescence and NIR-I photoacoustic imaging of orthotopic brain tumors. *Adv Mater.* 2018;30:1800766.
  25. Lu T, Chen F, Multiwfn. A multifunctional wavefunction analyzer. *J Comput Chem.* 2012;33:580–92.
  26. Lu T. A comprehensive electron wavefunction analysis toolbox for chemists. *Multiwfn J Chem Phys.* 2024;161:082503.
  27. Humphrey W, Dalke A, Schulten K. VMD: visual molecular dynamics. *J Mol Graph.* 1996;14:33–8. 27–8.
  28. Lee S, Karki R, Wang Y, Nguyen LN, Kalathur RC, Kanneganti T. AIM2 forms a complex with PIRIN and ZBP1 to drive PANoptosis and host defence. *Nature.* 2021;597:415–9.
  29. Zhong Z, Liang S, Sanchez-Lopez E, He F, Shalpour S, Lin X, Wong J, Ding S, Seki E, Schnabl B, Hevener AL, Greenberg HB, Kisseleva T, Karin M. New mitochondrial DNA synthesis enables NLRP3 inflammasome activation. *Nature.* 2018;560:198–203.
  30. Zhang Y, Su SS, Zhao S, Yang Z, Zhong C, Chen X, Cai Q, Yang Z, Huang D, Wu R, Han J. RIP1 autophosphorylation is promoted by mitochondrial ROS and is essential for RIP3 recruitment into necrosome. *Nat Commun.* 2017;8:14329.
  31. Lin J, Hu P, Wang Y, Tan Y, Yu K, Liao K, Wu Q, Li T, Meng Q, Lin J, Liu Z, Pu H, Ju H, Xu R, Qiu M. Phosphorylated NFS1 weakens oxaliplatin-based chemosensitivity of colorectal cancer by preventing PANoptosis. *Sig Transduct Target Ther.* 2022;7:54.

## Publisher's note

Springer Nature remains neutral with regard to jurisdictional claims in published maps and institutional affiliations.